Capture and chaotic scattering of a charged particle by a magnetic monopole under a uniform electric field

Kou Misaki and Naoto Nagaosa

Phys. Rev. E **98**, 052225 — Published 27 November 2018

DOI: 10.1103/PhysRevE.98.052225

Capture and chaotic scattering of a charged particle by magnetic monopole under uniform electric field

Kou Misaki,[1] Naoto Nagaosa[1,2]
[1] *Department of Applied Physics, The University of Tokyo, Bunkyo, Tokyo 113-8656, Japan*
[2] *RIKEN Center for Emergent Matter Science (CEMS), Wako, Saitama 351-0198, Japan*

(Dated: September 10, 2018)

Motivated by the realization of magnetic monopole of Berry curvature by the energy crossing point, we theoretically study the effect of magnetic monopole under a uniform electric field in the semiclassical wave packet dynamics, which is relevant to many physical situations such as relaxation through the diabolic point. We found that the competition between the backward scattering by the monopole magnetic field and the acceleration by the electric field leads to the bound state, i.e., capture of a particle near the monopole. Furthermore, the nonlinearity induced by the magnetic monopole leads to the chaotic behavior in the transient dynamics, i.e., the transient chaos. We computed characteristic quantities of the strange saddle which gives rise to the transient chaos, and verified that the abrupt bifurcation occurs as we tune the system parameter toward the parameter region in which the system is solvable.

I. INTRODUCTION

Since Dirac theoretically pointed out its possible existence by considering the 2π ambiguity of the phase of an electron wavefunction [1], magnetic monopole has attracted wide theoretical interests and appeared in many areas of physics [2–4]. In particular, magnetic monopole of Berry curvature [5] or synthetic gauge field [6, 7] appears both in real [8–10] and momentum [11–14] spaces, and drastically affects the transport property as it modifies the semiclassical equation of motion for the wave packet of particles [15–18].

Actually, the history of magnetic monopole [19–23] dates back to the late 1800s when Darboux and Poincaré theoretically studied the scattering problem of an electron by a magnetic monopole [24, 25]. This problem is known to be exactly solvable, and exhibits some unusual properties [22] (see Appendix A and B for the review of the exact solution). In this paper, we will show that, upon introducing the uniform electric field, the peculiar nature of this scattering problem leads to the chaotic dynamics, i.e., the chaotic scattering [26–31]. We note that, although the formulation itself is purely classical, our model can be viewed as the semiclassical approximation, i.e., taking into account of the first order in $\hbar$ expansion, of the wave packet dynamics in the multilevel system [32]. Here Berry curvature which appears in the form of the magnetic field is the quantum correction to the purely classical dynamics, and it is known that the energy crossing point acts as the magnetic monopole [5, 33], so our model can be viewed as the semiclassical approximation to the relaxation dynamics in the two level system, where the wave packet passes near the degenerate point.

II. MODEL

We numerically study the equation describing the dynamics of a particle under the influence of monopole magnetic field and the uniform electric field:

$$m\frac{d^2\vec{r}}{dt^2} = f\vec{e}_z + q_m q_e \frac{d\vec{r}}{dt}\times\frac{\vec{r}}{r^3}, \tag{1}$$

where m is the mass of particle, f is the uniform force along z direction, q_m and q_e are the magnetic charge of the monopole sitting at the origin and the electric charge of the particle, respectively. This equation has two conserved quantities, i.e., the energy and the angular momentum along z direction:

$$E = \frac{m}{2}(\dot{\vec{r}})^2 - fz, \quad J_z = m(x\dot{y} - y\dot{x}) - q_m q_e \frac{z}{r}, \tag{2}$$

where the second term of J_z comes from the angular momentum of the electromagnetic field. We can utilize J_z conservation to reduce one degree of freedom, as follows. The Lagrangian for our model can be written as

$$L = \frac{m}{2}(\dot{\rho}^2 + \dot{z}^2 + \rho^2\dot{\phi}^2) - q_m q_e \frac{z}{\sqrt{\rho^2+z^2}}\dot{\phi} + fz, \tag{3}$$

where (ρ, ϕ, z) represent the cylindrical coordinates, and the vector potential $A_\phi = -q_m q_e z/\sqrt{\rho^2+z^2}$ comes from the magnetic monopole at the origin. Since ϕ is the cyclic coordinate of the system, the conjugate momentum J_z, Eq. (2), is conserved. Then, we can construct the Routhian [34]:

$$\begin{aligned} R &= L - J_z\dot{\phi}|_{\dot{\phi}=(J_z+q_m q_e \frac{z}{\sqrt{\rho^2+z^2}})/(m\rho^2)} \\ &= \frac{m}{2}(\dot{\rho}^2 + \dot{z}^2) \\ &\quad - \frac{1}{2m\rho^2}\left(J_z + q_m q_e \frac{z}{\sqrt{z^2+\rho^2}}\right)^2 + fz. \end{aligned} \tag{4}$$

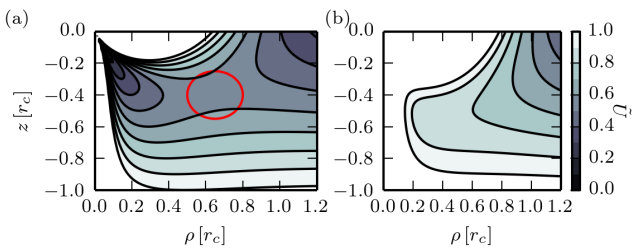

FIG. 1. The distribution of $U_{\rm eff}$ in (ρ, z) plane for (a) $J_z/(q_m q_e) = 0.9$, and (b) $J_z/(q_m q_e) = \sqrt{32/27} + 0.01$. The color represents the potential height $\tilde{U} \coloneqq U_{\rm eff}/(f r_c)$, where $r_c \coloneqq |q_m q_e|^{2/3}/(mf)^{1/3}$, as is shown in the right of (b). We can see the potential saddle as we highlighted with the red circle for (a), while the saddle disappears for (b).

The dynamics is now described by two degrees of freedom (ρ, z) and the potential energy is modified, as follows:

$$\begin{cases} m\dfrac{d^2 z}{dt^2} = -\dfrac{\partial U_{\rm eff}}{\partial z} \\ m\dfrac{d^2 \rho}{dt^2} = -\dfrac{\partial U_{\rm eff}}{\partial \rho}, \end{cases} \qquad U_{\rm eff} \coloneqq -fz + \frac{\left(J_z + \frac{q_m q_e z}{\sqrt{z^2+\rho^2}}\right)^2}{2m\rho^2}. \tag{5}$$

The form of the potential depends on the value of J_z, which is determined from the initial conditions according to Eq. (2). As we can see from Fig. 1 (a), there exists a potential saddle for particular parameter range of J_z. If we consider the dynamics of the particle starting from the initial position inside the potential pocket bounded by the saddle and the potential walls, the particle bounces back and forth inside the pocket, and eventually goes over the saddle. Therefore, the existence of the saddle and the potential pocket it bounds are the crucial ingredients for this scattering problem; We discuss about the condition for the existence of it in the next section.

Since the diverging magnetic field leads to the infinite cyclotron frequency, it invalidates the numerical calculation for the trajectory passing near the origin. To avoid this difficulty, we introduce the smeared magnetic charge:

$$p(\vec{r}) = \frac{1}{\xi^3\sqrt{\pi^3}} \int d\vec{R}\, e^{-\frac{|\vec{r}-\vec{R}|^2}{\xi^2}} q_m \delta(\vec{R}) = \frac{q_m e^{-\frac{r^2}{\xi^2}}}{\xi^3\sqrt{\pi^3}}. \tag{6}$$

The magnetic field produced by this magnetic charge is the same as the monopole for $r \gg \xi$, and converges to 0 as $r \to 0$.

III. RESULT

We performed the numerical calculation of Eq. (1) with the Runge-Kutta method and the implicit Tajima method [35]. We can regard the dynamics described by Eq. (1) as a scattering problem of a charged particle by magnetic monopole. There are two important physical observables: $t_{\rm pass}$, which is the time it takes for the particle to get out of the scattering region, which we define as $r \le 2r_c$ ($r_c \coloneqq |q_m q_e|^{2/3}/(mf)^{1/3}$), and $r_{\rm min} \coloneqq \min_t\{r(t)\}$, which determines whether our approximation of the point magnetic charge by the smeared one is good or not. We set the initial velocity to be zero, and vary $z(0) = z_0$ and $x(0) = x_0$ to adjust the incident velocity and the impact parameter, respectively, and set $q_m q_e < 0$. We show the result of the numerical calculation in Fig. 3. For small x_0 (small J_z) and small $|z_0|$ (small energy) region, we observed that $t_{\rm pass}$ becomes larger than the numerically accessible time region. This fact can be understood from the geometry of the effective potential Eq. (5): For this region, the particle cannot escape from the scattering region since the height of the potential saddle is higher than the initial energy; The condition for the existence of this region can be obtained as shown below.

If we vary the two parameters (x_0, z_0), $J_z(x_0, z_0)$ and $E_0(z_0)$ change and for small E_0 and large J_z, the region with $E \le E_0$ is separated and confined to the finite region, as we can see from Fig. 2(c), thereby leading to the infinite $t_{\rm pass}$. For smaller J_z, the two regions are connected by the saddle with the energy height $E_{\rm saddle} < E_0$, leading to finite $t_{\rm pass}$. To obtain the analytical expression of the boundary between these two cases in (J_z, E_0) plane, we observe that,

$$\begin{aligned} &U_{\rm eff} = E_0 \\ \Leftrightarrow &2\sin v \cos^2 v R^3 + 2\epsilon_0 \cos^2 v R^2 - (\sin v + \tilde{J}_z)^2 = 0, \end{aligned} \tag{7}$$

where $Z \coloneqq r_c z$, $P \coloneqq r_c \rho$, $R \coloneqq r_c r$, $Z = R\sin v$, $P = R\cos v$, $r_c = |q_m q_e|^{2/3}/(mf)^{1/3}$, $\tilde{J}_z \coloneqq J_z/(q_m q_e)$ and $\epsilon_0 \coloneqq E_0/(f r_c)$. The necessary condition for the merger of two separate region is that the discriminant for this third order polynomial for R is zero:

$$\sin^4 v + 2\tilde{J}_z \sin^3 v + \left(\tilde{J}_z^2 + \alpha\right)\sin^2 v - \alpha = 0, \tag{8}$$

where $\alpha \coloneqq 8\epsilon_0^3/27$. Furthermore, we impose the condition that the discriminant for this fourth order polynomial for $\sin v$ is zero:

$$\alpha^2(\alpha^3 + (3\tilde{J}_z^2+8)\alpha^2 + (3\tilde{J}_z^4 - 20\tilde{J}_z^2 + 16)\alpha + \tilde{J}_z^4(\tilde{J}_z^2 - 1)) = 0. \tag{9}$$

Solving this equation for α, we obtain five solutions. Choosing the relevant solution, we obtain

$$\epsilon_0 = \left(-\frac{9}{8}(8 + 3\tilde{J}_z) + \frac{9}{2}\frac{4 + 27\tilde{J}_z^2}{G} + \frac{9}{8}G\right)^{\frac{1}{3}}, \tag{10}$$

where G is given as

$$\left(64 - 1080\tilde{J}_z^2 - \frac{729\tilde{J}_z^4}{2} + \frac{3\sqrt{3}}{2}\sqrt{\tilde{J}_z^2(-32 + 27\tilde{J}_z^2)^3}\right)^{\frac{1}{3}}. \tag{11}$$

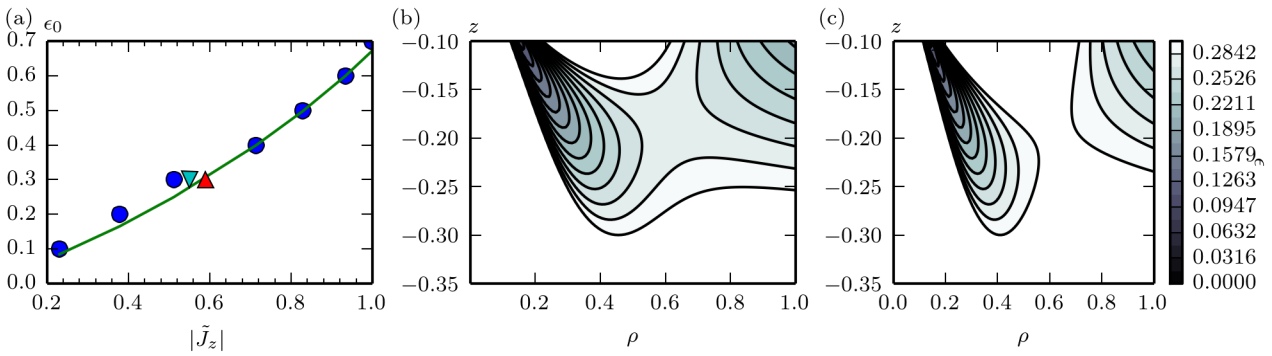

FIG. 2. (a) The boundary separating the trapping orbit and the escaping orbit. The dots are the result of the numerical calculation and the line represents the analytic expression Eq. (10). (b,c) The contour plot for the energy range $0 < \epsilon < \epsilon_0 = 0.3$ and $\tilde{J}_z = 0.55$ and 0.59 for (b) and (c), respectively. The parameter values for (b) and (c) are shown by the blue down triangle and red up triangle in (a), respectively.

The plot of this curve is shown by the solid line in Fig. 2(a). In addition, we obtain the value of J_z where the saddle point of the potential energy vanishes: Above $\tilde{J}_z^2 = 32/27$, the right hand side of Eq. 10 becomes complex, meaning that there is no saddle in the potential energy. Since the chaotic scattering is caused by the pocket of energy minimum bounded by the saddle, we expect no chaotic scattering above this J_z, so we concentrate on the dynamics for this range of J_z.

In addition, we can see the complicated peak structure in the region with small impact parameter, and as is shown in Fig. 4, each peak has a fractal structure, and the scattering angle Θ, which is the relative angle between the initial and the final velocity, varies very wildly near this peak structure. We show the dynamics at each hierarchy of the fractal in Fig. 5. We checked the convergence of the peak structure and the small error of conserved quantities, so this peak structure is not an artifact of the finite precision of the numerical calculation. Actually, this fractal structure of $t_{\rm pass}$ is a characteristic feature of the chaotic scattering [30, 31], which is the representative example of the transient chaos of Hamiltonian systems [36, 37].

To understand why the chaotic scattering occurs and the multiple peaks for each z_0 is observed, it is convenient to go back to $f = 0$ limit of Eq. (1). As we mentioned in the introduction, this model is exactly solved. Among some peculiar characteristics, one notable feature is the impact parameter (x_0) dependence of the scattering angle: There are multiple backscattering points (so-called glory scattering) located at $q_e q_m/(mvx_0) = \sqrt{4n^2-1}$ ($n = 1, 2, \dots$), where v represents the initial velocity [38, 39]. This is in sharp contrast to the scattering angle in the Rutherford scattering which has a monotonic impact parameter dependence. If we regard each backscattering point as the potential hill, the situation is formally similar to the scattering problem by multiple scatterer, which is known to exhibit the chaotic behavior at the transient time scale [30, 31]. Moreover, for fixed z_0 there

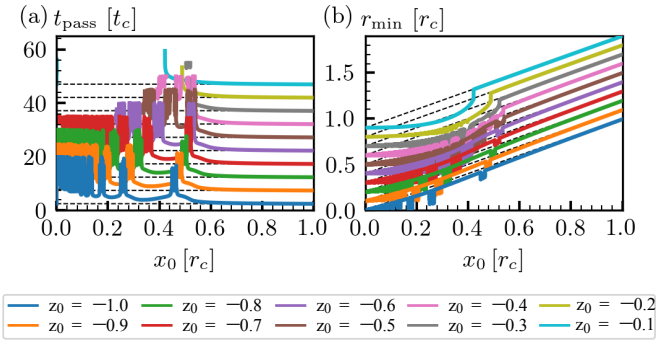

FIG. 3. The plot of the time when the particle get out of the scattering region $r \le 2r_c$ ($t_{\rm pass}$) and the minimum value of $r(t)$ ($r_{\rm min} := \min_t(r(t))$), for the initial position $(x_0, 0, z_0)$. Here $r_c := |q_m q_e|^{2/3}/(mf)^{1/3}$ and $t_c := (m|q_m q_e|)^{1/3}/f^{2/3}$. The numerical calculation was done with an implicit Tajima method. The black dashed line represent the values without the monopole magnetic field. Note that each plot is shown with an offset. The values of the offset are given by the values of the dashed line at $x_0 = 0$. For small x_0 and z_0, $t_{\rm pass}$ is larger than $t/t_c = 20$, and the plot of $t_{\rm pass}$ at these values are not shown.

are infinitely many x_0 where the particle is backscattered, and this leads to infinitely many well-separated peak structures (see Appendix C).

The chaotic scattering can be understood as a consequence of the fractional dimension of the saddle induced by the horseshoe mapping [40]. The fact that the saddle has a fractal dimension has a drastic consequence on the physical quantities: The dimension of generic crossing of the stable manifold of the saddle and the one parameter family of initial conditions in the phase space becomes fractional. As a result, at each intersection, the time it takes for the particle to get out of the scattering region ($t_{\rm pass}$) is infinite, so $t_{\rm pass}$ has a peak on the set with a fractional dimension. The dimension

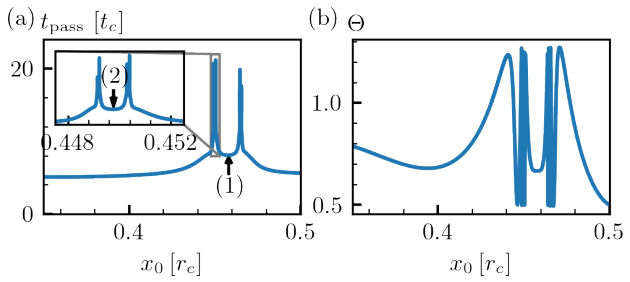

FIG. 4. (a) The peak structure of $t_{\rm pass}$ around $x_0/r_c \cong 0.45$ at $z_0/r_c = -1$. The inset shows the detailed peak structure of the left peak, and we can clearly see the self-similarity of the peak. We showed (1) and (2), which is the parameter point we take for the dynamics shown in Fig. 5. We define the parameter points (n) for all n larger than 2 for finer structures in the same way. (b) The rapid variation of $\Theta := \cos^{-1}(v_z(t_{\rm pass})/\sqrt{\vec{v}(t_{\rm pass})\cdot\vec{v}(t_{\rm pass})})$ near the fractal peak, which is the characteristic feature of the chaotic scattering [30, 31].

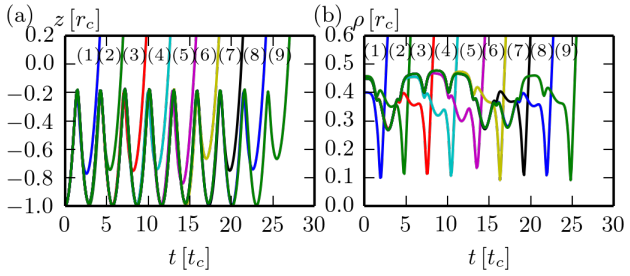

FIG. 5. The plots of (a) $z(t)$ and (b) $\rho(t)$. The value of x_0 at (n) is defined in Fig. 4. We can see the correspondence between the number of the oscillation and the number of the hierarchy.

of the crossing can be calculated as follows [41]: Our model is the Hamiltonian system with two degrees of freedom (Eq. (5)). Within each energy shell, the dimension of the phase space is three. Noting that Eq. (5) has time reversal symmetry, the dimensions of the stable and the unstable manifold are the same. Since the dimension of the intersection of the two subsets S_1 and S_2 in the d dimensional manifold ($d = 3$ in our case) is given by $D(S_1 \cap S_2) = D(S_1) + D(S_2) - d$, where $D(S)$ represents the dimension of S, and the saddle is given by the intersection of the stable and the unstable manifold, $D(S_{\rm st}) = (D(S_{\rm sad}) + 3)/2$, where $S_{\rm sad}$ and $S_{\rm st}$ represent the saddle and the stable manifold of the saddle. Therefore, the dimension of the crossing, which we refer to as the fractal dimension, is given by $d_{\rm fra} = 1 + D(S_{\rm st}) - 3 = (D(S_{\rm sad}) - 1)/2$.

Concerning the dynamics on the saddle, the positivity of the Lyapunov exponent itself does not immediately imply the chaotic behavior, which can be quantitatively understood from the following Kantz-Grassberger formula

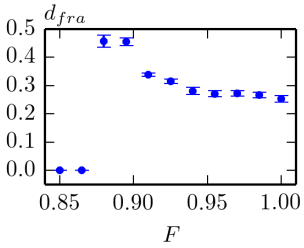

FIG. 6. The abrupt bifurcation observed by varying the force term toward zero. $F = f\tilde{r}_c/E$ is the dimensionless force parameter, where $\tilde{r}_c = |q_m q_e|/\sqrt{mE}$ and E is the total energy of the particle. $F = 1$ corresponds to the original parameter, and $F = 0$ corresponds to the solvable, zero force limit. We can see that the fractal dimension abruptly drops to zero around $F \sim 0.87$. The value of F used to calculate the quantities discussed in the main text corresponds to $F = 1$.

[31, 37, 42, 43]: $\sum_{\lambda_i>0}\lambda_i = \kappa + h_{\rm KS}$, where λ_is are the Lyapunov exponents of the invariant set, κ is the escape rate, i.e., $\kappa := \lim_{T\to\infty} -(1/T)\ln(N(T)/N(0))$ ($N(T)$ is the number of particles remaining in the scattering region at $t = T$), and $h_{\rm KS}$ is the Kolmogorov-Sinai entropy, of which nonzero value implies the chaos. This equation represents the fact that the instability of the invariant set (Lyapunov exponent) leads to two phenomena: The escape of the particle from the scattering region and the growth of the information which is the characteristic feature of the chaos. As we can see, positive λ_i with $h_{\rm KS} = 0$ is possible because of the finite escape rate κ in contrast to the case with the attractor. For the numerical calculation, the following Young's formula [43, 44] is useful: For the Hamiltonian system with two degrees of freedom, it is $h_{\rm KS} = \lambda(D_1 - 1)/2$, where D_1 is the information dimension in 3D phase space and is defined by

$$D_1 := \lim_{q\to 1} D_q := \lim_{q\to 1}\lim_{\delta\to 0}\frac{1}{q-1}\frac{\log\sum_i p_i^q}{\log\delta}, \qquad (12)$$

where δ is the linear size of the box we use to divide the phase space to define the measure p_i, and D_q is the Rényi dimension. Compared to the box counting dimension of the invariant set (D_0), the information dimension reflects the property of the dynamics on the set through the invariant measure p_i.

As is explained above, the information of the saddle which characterizes the chaotic behavior can be understood from the following quantities: κ, λ_i, D_0, D_1 and $h_{\rm KS}$. In the following, we calculate characteristic quantities of the fractal peak for $z_0 = -1$ near $x_0 = 0.45$ to confirm that what we found is transient chaos [31].

First, we calculate the uncertainty exponent [37] (We defined $|t_{\rm pass}(x_0 + \epsilon) - t_{\rm pass}(x_0)| > 0.5$ as the uncertain pair [45].). We obtained $d_{\rm fra} = 1 - d_{\rm unc} = 0.259 \pm 0.008$. We calculated this exponent for different values of the dimensionless force parameter $F = f\tilde{r}_c/E$, where $\tilde{r}_c = |q_m q_e|/\sqrt{mE}$, with the total energy E fixed. $F = 1$ limit corresponds to the original model Eq. (1) with

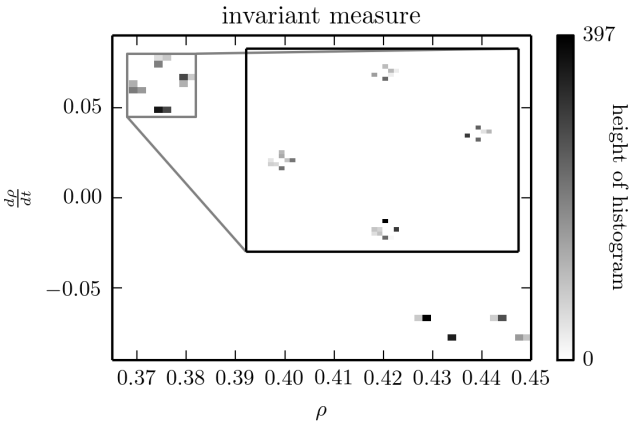

FIG. 7. The invariant measure of the strange saddle on the Poincaré section defined by $z = -0.5r_c$ and $v_z > 0$, obtained by the PIM-triple method [31, 47]. The number of points on Poincaré section obtained from the single trajectory is 3403, and we divide $(\rho, d\rho/dt)$ plane into 50×50 boxes to calculate the histogram. The color represents the height of the histogram, as is shown in the right of the figure.

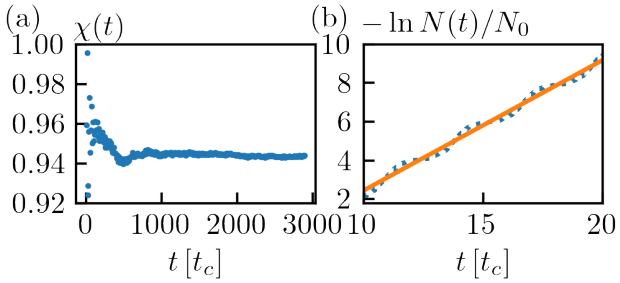

FIG. 8. The calculation of the (a) Lyapunov exponent and (b) escape rate. (a) We calculate $\chi(t)$ by evolving the two nearby phase space points and measure the deviation α_i after the time τ_i to obtain $\chi(t) = (1/\sum_i \tau_i)\sum_i \alpha_i$, of which we obtain the Lyapunov exponent from the limiting value [31, 36]. (b) The dotted line represents the numerically obtained number of surviving particles as a function of time, and the solid line is the fitting curve. The slope of the curve is the escape rate.

$\vec{r}(0) = (x_0, 0, -\tilde{r}_c)$ and $\vec{v}(0) = \vec{0}$, while $F = 0$ corresponds to $f = 0$ in Eq. (1) (i.e., the solvable limit [22]) with $\vec{r}(0) = (x_0, 0, -\tilde{r}_c)$ and $\vec{v}(0) = (0, 0, \sqrt{2E/m})$ [46]. We found that the abrupt bifurcation similar to the potential scattering problem [31] occurs around $F \sim 0.87$, see Fig. 6.

Secondly, we calculate the invariant measure of the strange saddle on the Poincaré section defined by $z = -0.5r_c$. We note that our system has two degrees of freedom with the energy conservation, Eq. (5). Accordingly, the dimension of the Poincaré section is $3 - 1 = 2$ (Remember that the phase space dimension is 3.), and we take the coordinate as $(\rho, d\rho/dt)$, where $\rho = \sqrt{x^2 + y^2}$. The result is shown in Fig. 7. From this invariant measure, we can calculate the Rényi dimension D_q in the three dimensional phase space by adding 1 (which corresponds to the direction of time evolution) to the fractal dimension of the saddle on the Poincaré section, defined in Eq. (12). We obtain $D_2 = 1.51 \pm 0.02$, $D_1 = 1.52 \pm 0.02$ and $D_0 = 1.54 \pm 0.01$, so D_0 and D_1 are almost the same within the error in our model.

Finally, we calculate the Lyapunov exponent λ and the escape rate κ, see Fig. 8. We note that, since our system is the Hamiltonian system with two degrees of freedom, the energy conservation leads to zero Lyapunov exponent, and the direction of the flow corresponds to another direction with zero Lyapunov exponent. In addition, since the symplectic structure leads to the symmetric distribution of the Lyapunov exponents around zero, the calculation of the one positive Lyapunov exponent is enough. We obtained $\lambda = 0.9437 \pm 0.0002$ and $\kappa = 0.676 \pm 0.001$. If we substitute these values to the Kantz-Grassberger formula with Young's formula, we obtain the information dimension of the saddle $D_1 = 1 + 2(1 - \kappa/\lambda) = 1.568 \pm 0.002$, which is in accordance with the result of calculated information dimension of the saddle D_1. In addition, from Young's formula, we obtain $h_{\mathrm{KS}} = 0.268 \pm 0.001$. Also, the value of D_0 is consistent with the uncertainty exponent by the formula $D_0 = 1 + 2d_{\mathrm{fra}} = 1.52 \pm 0.02$.

Next, we discuss the stability of the chaotic behavior against the dissipative perturbation [48–50], i.e., $-\eta\dot{\vec{r}}$ term in the right hand side of Eq. (1), see Fig. 9 and 10. The effect of dissipation on the transient chaos has been studied and is termed as "doubly transient chaos" [51, 52]. The two notable features in their models are as follows [51, 52]: The dissipation leads to the exponential increase of the escape rate, and the fractal dimension decreases monotonically for finer scale ($\epsilon \to 0$). The former one is in accordance with our model, while the latter one is in stark contrast to our model: As is shown in Fig. 10 (b), the escape rate suddenly starts to increase around $t \sim 150$ after the long plateau $\kappa \sim 0$, in accordance to the expression of the escape rate in the presence of dissipation: $\kappa = \exp(\gamma t + \ln(\kappa_0))$ [51]; We found that as we look finer scale, the fractal dimension rapidly grows and saturate at 1, see Fig. 10. The fractal dimension may eventually decrease if we look much finer scale [51]. Also we note that this behavior may be due to the peculiarity of our model. Indeed we observed similar kind of monotonic increase of the fractal dimension in a slightly modified model in the absence of dissipation (see Appendix C), where we can attribute the increase of the fractal dimension to the infinite number of backscattering points. We note that this behavior strongly depends on the way we regularize the monopole singularity, since r_{min} is very close to zero around the peaks, see Fig. 9. We also found as we further increase the dissipation, t_{pass} becomes smooth, and the chaos disappears.

We further verified the stability against the perturbation which breaks J_z conservation, i.e., the deformation

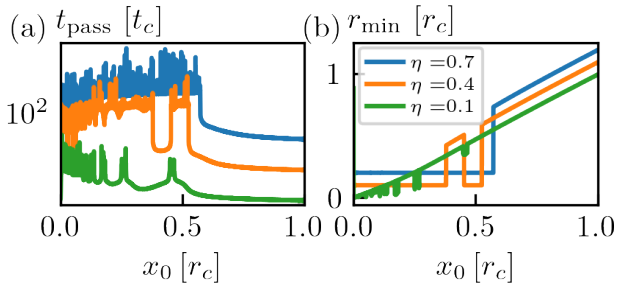

FIG. 9. The plots of the (a) $t_{\rm pass}$ and (b) $r_{\rm min}$. The value of η is shown above (a). As we can see, as we increase the strength of the dissipation, the fractal peak becomes broad with rapid variation and $r_{\rm min}$ is very close to zero, which means that this behavior strongly depends on the way we regularize the monopole singularity. Note that the plots are shifted upward.

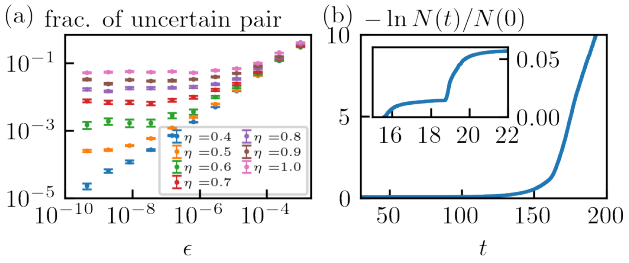

FIG. 10. The plots of the (a) fraction of uncertain pair, and (b) the minus logarithm of the number of surviving particles. (a) As we can see, the uncertainty exponent $d_{\rm unc}$ given by the slope in (a) (the fractal dimension given by $d_{\rm fra} = 1 - d_{\rm unc}$) decreases (increases) as we see finer scale ($\epsilon \to 0$), which is in stark contrast to the doubly transient chaos. The value of η is as is shown in the legend. (b) The inset shows the early time behavior, which shows linear behavior in time. After some time (around $t = 100$), the number of escaping particles suddenly increases, which means the monotonic increase of the escape rate.

of the mass along x direction. We calculated the fractal dimension and found that it remains finite upon deformation, see Fig. 11. From these results, we believe that the chaotic behavior we found can be observed in the experiments where the various perturbations exist.

IV. SUMMARY AND DISCUSSION

We found the fractal peak structure in $t_{\rm pass}$ in the scattering problem of a charged particle by magnetic monopole in the presence of a uniform electric field, and verified it is the consequence of the fractal nature of the saddle by calculating the quantities which characterize the saddle. Although our model have a single scatter, i.e., the monopole, the unusual nature of the scattering angle effectively leads to the scattering problem between

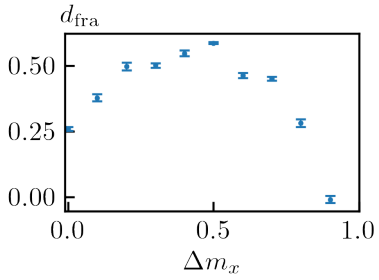

FIG. 11. The fractal dimension against the mass deformation, Δm_x. $\Delta m_x = m_x - 1$ and $\Delta m_x = 0$ is the original parameter. By increasing Δm_x, the mass along x direction becomes large and the system becomes more and more anisotropic.

multiple potential hills. We observed two bifurcation routes (1) by varying the electric field toward zero, where the model is solvable; (2) by introducing the dissipation, through the intermediate region where the fractal dimension monotonically increase as the scale becomes finer. We clarified the stability of the chaotic behavior against the perturbations which exist in the real experiments.

In addition, we found the divergence of $t_{\rm pass}$, i.e., the capture of the particle by the monopole. It is caused by the fact that the region which is accessible by the particle is bounded near the monopole, and we analytically derived the parameter region where the capturing occurs. The capturing observed here may serve as a mechanism of the bottleneck effect where the relaxation of the excited state toward the ground state in Born-Oppenheimer energy landscape is slowed down by the Berry curvature coming from the diabolic point.

The important future work is the detailed discussion of the symmetry breaking deformation, i.e., the mass deformation by extending the discussion of the "geometric magnetism" and "deterministic friction" [16, 53] using the invariant measure on the saddle [43].

ACKNOWLEDGMENTS

The authors thank H. Ishizuka and X.-X. Zhang for useful discussions. This work was supported by JSPS KAKENHI Grant Number JP18J21329 (K.M.), and JSPS KAKENHI Grant Number JP26103006, JP18H03676, and ImPACT Program of Council for Science, Technology and Innovation (Cabinet office, Government of Japan), and JST CREST Grant Numbers JPMJCR16F1, Japan (N.N.).

Appendix A: Dynamics of charged particle in the presence of monopole

Here, we review the analytic solution in the case of $f = 0$ [24, 25, 54], for completeness. The equation of

motion is,

$$m\ddot{\vec{r}} = q_e q_m \frac{\dot{\vec{r}} \times \vec{r}}{r^3}. \tag{A1}$$

By taking the inner product with $\dot{\vec{r}}$, and the outer product with $\vec{r}$, we obtain four conserved quantities:

$$E := \frac{m}{2}(\dot{\vec{r}})^2, \quad \vec{J} := m\vec{r}\times\dot{\vec{r}} - q_e q_m \frac{\vec{r}}{r} =: \vec{L} - q_e q_m \frac{\vec{r}}{r}. \tag{A2}$$

Among them, the independent conserved quantities are E, J_z and $|\vec{J}|$. If we take the inner product with $\vec{r}$ and Eq. (A1), we obtain $\vec{r}\cdot\ddot{\vec{r}} = 0$, so

$$\begin{aligned} &\frac{d^2 r^2}{dt^2} = 2(\dot{\vec{r}})^2 = \frac{4E}{m}, \\ &\therefore r(t) = \sqrt{(\vec{v}_0)^2 t^2 + 2(\vec{r}_0\cdot\vec{v}_0)t + (\vec{r}_0)^2} = |\vec{v}_0 t + \vec{r}_0|, \end{aligned} \tag{A3}$$

where $\vec{r}(0) = \vec{r}_0$ and $\dot{\vec{r}}(0) = \vec{v}_0$. We assume that $\vec{r}_0$ is not parallel to $\vec{v}_0$. Here, we take $\vec{J}$ along the z direction and take the spherical coordinate (r, θ, ϕ). Then,

$$\frac{\vec{J}\cdot\vec{r}}{r} = -q_e q_m \Leftrightarrow \cos\theta = \frac{-q_e q_m}{J} = \frac{-q_e q_m}{\sqrt{L^2 + (q_e q_m)^2}}. \tag{A4}$$

Finally, we take the inner product of $\vec{J}$ and $\vec{L}$:

$$\vec{J}\cdot\vec{L} = J^2 - (q_e q_m)^2 \Leftrightarrow L_z = J\sin^2\theta. \tag{A5}$$

Since $L_z = mr^2\sin^2\theta\dot{\phi}$, we obtain

$$\begin{aligned} &\dot{\phi} = \frac{J}{mr^2}, \\ &\therefore \phi(t) = \frac{1}{\sin\theta}\left[\tan^{-1}\left(\frac{(\vec{v}_0)^2 t + \vec{r}_0\cdot\vec{v}_0}{|\vec{r}_0\times\vec{v}_0|}\right)\right. \\ &\qquad\left. - \tan^{-1}\left(\frac{\vec{r}_0\cdot\vec{v}_0}{|\vec{r}_0\times\vec{v}_0|}\right)\right] \end{aligned} \tag{A6}$$

Combining Eqs. (A3), (A4) and (A6), we obtained the analytical solution. From Eq. (A4), we can see that the the motion of the particle is restricted on the cone oriented along $\vec{J}$ with the angle $\theta_0 = \cos^{-1}(-q_e q_m/J)$. Here we note that the motion is similar to the motion in the absence of the monopole in two aspects: the motion is restricted to the two dimensional plane (i.e., the cone), and the trajectory on that plane is geodesic. To see the first aspect in more detail, we fix $\vec{r}_0$ and $\vec{v}_0$ and show the form of the cone in Fig.12. Here, we let $\vec{L}(0)$ along the z axis to show the difference between $q_e q_m < 0$ and $q_e q_m > 0$ cases (Note the difference of the coordinate system from the analytic solution.). We consider the process where we start from the $q_e q_m = 0$ and gradually increase $|q_e q_m|$. That results in the two modifications: The direction of the total angular momentum tilts toward the position of the particle, $\vec{r}_0$, and the surface where the trajectory of

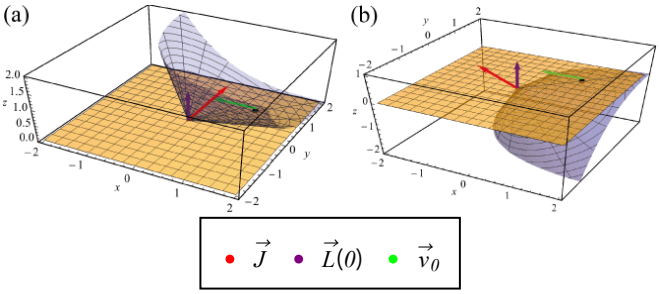

FIG. 12. The cone on which the trajectory of the particle lies (shown blue), in the case of (a) $q_e q_m < 0$ and (b) $q_e q_m > 0$. We can see the direction of the tilting of $\vec{J}$ and the direction of the bending of $x-y$ plane into the cone differ in the two cases. The black dot represents the initial position of the particle, and the red, purple and green arrows represent $\vec{J}$, $\vec{L}(0)$ and $\vec{v}_0$, respectively. We took the z axis along $\vec{L}(0)$ direction, which coincides with $\vec{J}$ in the case of $q_e q_m = 0$, and the orange plane represents $x-y$ plane.

the particle lies is bent from the $x-y$ plane into the cone. We note that, since the $x-y$ plane is tangential to the cone at $\vec{r}_0$ and the initial velocity is along the $x-y$ plane, the particle will not get out of the cone [46]. Since the trajectory of the particle at $q_e q_m = 0$ is the geodesic on the $x-y$ plane, we expect the motion of the particle on the cone is also the geodesic. To verify that this is correct, we define χ as the angle between $\vec{r}_0$ and $\vec{v}_0$. Then,

$$\frac{\vec{r}_0\cdot\vec{v}_0}{|\vec{r}_0\times\vec{v}_0|} = \cot\chi = \tan\left(\frac{\pi}{2} - \chi\right), \tag{A7}$$

so from Eq. (A6),

$$\begin{aligned} \frac{(\vec{v}_0)^2 t + \vec{r}_0\cdot\vec{v}_0}{|\vec{r}_0\times\vec{v}_0|} &= \tan\left(\sin\theta\phi(t) + \frac{\pi}{2} - \chi\right) \\ &= -\cot(\sin\theta\phi(t) - \chi), \end{aligned}$$

therefore,

$$\begin{aligned} &\frac{(\vec{v}_0)^2 r(t)^2 + (\vec{r}_0\cdot\vec{v}_0)^2 - (\vec{v}_0)^2(\vec{r}_0)^2}{|\vec{r}_0\times\vec{v}_0|^2} \\ &\qquad = \cot^2(\sin\theta\phi(t) - \chi) \quad (\because \text{Eq. (A3)}) \\ &\Leftrightarrow \frac{(\vec{v}_0)^2 r(t)^2}{|\vec{r}_0\times\vec{v}_0|^2} = \cot^2(\sin\theta\phi(t) - \chi) + 1 \\ &\therefore r(t)\sin(\chi - \sin\theta\phi(t)) = r_0\sin\chi. \end{aligned} \tag{A8}$$

To understand this equation, we expand the cone to obtain the development, and consider the two dimensional motion on that. Then, the quantity $\sin\theta\phi(t)$ represents the angle between $\vec{r}_0$ and $\vec{r}(t)$ in the development of the cone. Since χ represents the angle between $\vec{r}_0$ and $\vec{v}_0$, the above equation can be rewritten as:

$$\vec{v}_0\cdot\vec{r}(t) = \vec{v}_0\cdot\vec{r}_0 \quad \text{on the development of the cone.} \tag{A9}$$

It means that the motion of the particle is a straight line on the development. In other words, the trajectory is

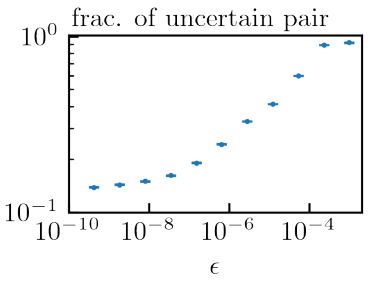

FIG. 13. The fraction of uncertain pair. As we can see, the uncertainty exponent $d_{\rm unc}$ given by the slope (the fractal dimension given by $d_{\rm fra} = 1 - d_{\rm unc}$) decreases (increases) as we see finer scale ($\epsilon \to 0$). The calculation was done for the peak around $L_0 = 0.6$ with $A = B = 10$, see Fig. 14(b).

geodesic for the flat metric induced by (locally) identifying the development of the cone with the two dimensional Euclidean space. In this sense, the trajectory is still "straight", although in three dimensional space it looks complicated.

One important feature which is relevant for the main text is Eq. (A3). It means that the monopole does not attract the particle to cause the delay of the passing of the particle near the origin.

Appendix B: Hamilton-Jacobi equation

Here we solve $f = 0$ case with the Hamilton-Jacobi method, which may serve as a good starting point for further analysis with the perturbation theory. The Hamiltonian for Eq. (3) obtained by the Legendre transformation is the following:

$$H = \frac{p_r^2}{2m} + \frac{1}{2mr^2}\left[p_\theta^2 + \frac{1}{\sin^2\theta}\left(p_\phi + q_m q_e \cos\theta\right)^2\right]. \tag{B1}$$

The Hamilton-Jacobi equation for this Hamiltonian is

$$\begin{aligned}
&\frac{\partial S}{\partial t} + H\left(q_i, \frac{\partial S}{\partial q_i}\right) = 0 \\
\Leftrightarrow &\frac{\partial S}{\partial t} + \frac{1}{2m}\left(\frac{\partial S}{\partial r}\right)^2 \\
&+ \frac{1}{2mr^2}\left[\left(\frac{\partial S}{\partial \theta}\right)^2 + \frac{1}{\sin^2\theta}\left(\frac{\partial S}{\partial \phi} + q_m q_e \cos\theta\right)^2\right] = 0.
\end{aligned} \tag{B2}$$

Since the energy is conserved, ϕ is the cyclic coordinate, and r and θ are separable, we put $S = -\epsilon t + W_r(r) + W_\theta(\theta) + \alpha_\phi \phi$ to obtain

$$\left(\frac{\partial W_\theta}{\partial \theta}\right)^2 + \frac{1}{\sin^2\theta}\left(\alpha_\phi + q_m q_e \cos\theta\right)^2 = \alpha_\theta^2 - (q_e q_m)^2, \tag{B3}$$

$$\left(\frac{\partial W_r}{\partial r}\right)^2 + \frac{\alpha_\theta^2 - (q_e q_m)^2}{r^2} = 2m\epsilon, \tag{B4}$$

where α_θ and α_ϕ corresponds to $|\vec{J}|$ and J_z, respectively. At this point, ϵ, α_θ, and α_ϕ are constants of motion. These equations can be transformed to

$$W_\theta = -\int d\theta \sqrt{\alpha_\theta^2 - (q_e q_m)^2 - \frac{1}{\sin^2\theta}(q_e q_m \cos\theta + \alpha_\phi)^2}, \tag{B5}$$

$$W_r = \int dr \sqrt{2m\epsilon - \frac{\alpha_\theta^2 - (q_e q_m)^2}{r^2}}, \tag{B6}$$

where we chose the minus sign for W_θ just for convenience. Then, we calculate $\beta_i(q_i, \alpha_i) := \frac{\partial S}{\partial \alpha_i}$, which are canonically conjugate to α_i and are the remaining constants of motion. After a bit long but straightforward calculation, we obtain

$$\begin{aligned}
\beta_\phi &:= \frac{\partial S}{\partial \alpha_\phi} \\
&= \phi - \frac{\pi}{2} + \arctan\left[\frac{\cos A \sin i - \cos i \sin A \sin\psi}{\cos\psi \sin A}\right],
\end{aligned} \tag{B7}$$

$$\begin{aligned}
\beta_\theta &:= \frac{\partial S}{\partial \alpha_\theta} \\
&= \frac{1}{\sin A}\left(\frac{\pi}{2} - \arctan\left[\sqrt{\frac{2m\epsilon r^2}{\alpha_\theta^2 \sin^2 A} - 1}\right]\right) + \psi,
\end{aligned} \tag{B8}$$

$$\beta_0 := \frac{\partial S}{\partial \epsilon} = -t + \sqrt{\frac{m}{2\epsilon}}\sqrt{r^2 - \frac{\alpha_\theta^2 \sin^2 A}{2m\epsilon}}, \tag{B9}$$

where

$$\cos\theta = \sin A \sin i \sin\psi + \cos A \cos i, \tag{B10}$$

$$\cos A := \frac{-q_e q_m}{\alpha_\theta}, \tag{B11}$$

$$\cos i := \frac{\alpha_\phi}{\alpha_\theta}. \tag{B12}$$

By solving Eqs. (B7), (B8) and (B9) for (r, ψ, ϕ), noting that we are free to add $\Delta S(\alpha_i)$ to S to shift each β_i by any function of α_i, we obtain

$$r(t) = \sqrt{\frac{2\epsilon}{m}(t + \beta_0)^2 + \frac{\alpha_\theta^2 \sin^2 A}{2m\epsilon}}, \tag{B13}$$

$$\psi(t) = \beta_\theta + \frac{1}{\sin A}\arctan\left[\frac{2\epsilon}{\alpha_\theta \sin A}(t + \beta_0)\right], \tag{B14}$$

$$\phi(t) = \beta_\phi - \arctan\left[\frac{\cos A \sin i - \cos i \sin A \sin\psi(t)}{\cos\psi(t) \sin A}\right]. \tag{B15}$$

Note that if we substitute

$$\beta_0 = \frac{\vec{v}_0 \cdot \vec{r}_0}{(v_0)^2}, \tag{B16}$$

$$\beta_\theta = -\frac{1}{\sin A} \arctan\left[\frac{2\epsilon\beta_0}{\alpha_\theta \sin A}\right], \tag{B17}$$

into Eqs. (B13) and (B14), we reproduce Eqs. (A3) and (A6).

Appendix C: On the peak structure of t_{pass}

To understand the peak structure of t_{pass}, we consider the following toy model which can be smoothly deformed to our model: We put the potential barrier at $z = -A < 0$ plane, and consider the motion of the particle bouncing back and force between this potential barrier and the magnetic monopole at the origin. We start from the limit where the barrier is step-like and far from the origin, and smoothly vary the position and thickness of the barrier to reach the limit where the potential can be regarded as the one imitating the uniform electric field.

More concretely, we consider the potential of the form $U(z) = 1 - \tanh((z + A)/B)$, where A represents the position of the wall and B represents the width of the slope of the potential. We set the initial condition as $\vec{v}_0 = \vec{0}$ and $(x_0, y_0, z_0) = (0, 0, -A)$, and calculated $L = |\vec{r} \times \vec{v}|$ and v_z at the first two intersections with the Poincaré section at $z = -A + 1$ with $v_z > 0$. We note that, because of J_z and E conservation, the effective phase space degrees of freedom is three, so the Poincaré map is defined as $(L_n, v_{z,n}) \to (L_{n+1}, v_{z,n+1})$. We show L_1, t_{pass} and $\Theta := \arccos(\vec{v}_0 \cdot \vec{v}_1)$ as a function of L_0 in Fig. 14. As we can see, complicated peak structure is observed near the point where $L_0 = L_1$ holds. We note that near these regions, $\Theta \sim 0$, so we speculate that the Poincaré map can be approximated as $(L_n) \to (L_{n+1})$ at least for this initial regime. By considering the web diagram in Fig. 14(a), we can understand the complicated peak structure of Fig. 14(b): The particles which start from the points sandwiched between the crossing points of blue and black lines goes to smaller L region, and among them, some particles again get to the region sandwiched between the crossing points and mapped to smaller L region, and so on. Therefore, we conclude that the complicated peak structure of t_{pass} (Fig. 14(b)) and the monotonic increase of the fractal dimension as a function of scale (Fig. 13) is caused by infinite number of backscattering points, around which L is mapped to smaller value.

As we deform A and B to reach the model which is similar to our model with uniform electric field, these peak structure evolves into the fractal peak, see Fig. 15. So, from the argument above, we speculate that the multiple backscattering points plays the role of the potential hills in the usual chaotic scattering [30, 31], thereby producing the infinite number of symbol sequence by labeling each backscattering points by integers.

Appendix D: The change of U_{eff} from the variation of f

We consider the one parameter family which connects the equation of motion for Eq. (5) where $U(\rho, z) = -fz$ to the one where $U(\rho, z) = 0$, the solvable limit. We define $\tilde{r}_c = |q_m q_e|/\sqrt{mE}$ and $\tilde{t}_c = |q_m q_e|/E$. Then the equation of motion can be rewritten as

$$\begin{cases} \dfrac{d^2\tilde{Z}}{d\tilde{\tau}^2} = -\dfrac{\partial \tilde{U}_{\text{eff}}}{\partial \tilde{Z}} \\ \dfrac{d^2\tilde{P}}{d\tilde{\tau}^2} = -\dfrac{\partial \tilde{U}_{\text{eff}}}{\partial \tilde{P}}, \end{cases} \tag{D1}$$

$$\tilde{U}_{\text{eff}} := -F\tilde{Z} + \frac{1}{2}\left(\frac{J_z}{q_m q_e} + \frac{\tilde{Z}}{\sqrt{\tilde{Z}^2 + \tilde{P}^2}}\right)^2,$$

where $\tilde{Z} = z/\tilde{r}_c$, $\tilde{P} = \rho/\tilde{r}_c$, $\tilde{\tau} = t/\tilde{t}_c$ and $F = f\tilde{r}_c/E$. The change of U_{eff} as a function of F is shown in Fig. 16.

[1] P. A. M. Dirac, Proc. R. Soc. Lond. A **133**, 60 (1931).
[2] G. 't Hooft, Nuclear Physics, B **79**, 276 (1974).
[3] A. M. Polyakov, ZhETF Pisma Redaktsiiu **20**, 430 (1974).
[4] C. Castelnovo, R. Moessner, and S. L. Sondhi, Nature **451**, 42 (2008).
[5] M. V. Berry, Proc. R. Soc. Lond. A **392**, 45 (1984).
[6] J. Dalibard, F. Gerbier, G. Juzeliūnas, and P. Öhberg, Reviews of Modern Physics **83**, 1523 (2011).
[7] N. Goldman, G. Juzeliūnas, P. Öhberg, and I. B. Spielman, Reports on Progress in Physics **77**, 126401 (2014).
[8] P. Zhang, Y. Li, and C. P. Sun, The European Physical Journal D - Atomic, Molecular, Optical and Plasma Physics **36**, 229 (2005).
[9] J. Ruseckas, G. Juzeliūnas, P. Öhberg, and M. Fleischhauer, Phys. Rev. Lett. **95**, 010404 (2005).
[10] M. W. Ray, E. Ruokokoski, S. Kandel, M. Möttönen, and D. Hall, Nature **505**, 657 (2014).
[11] S. Murakami, New Journal of Physics **9**, 356 (2007).
[12] X. Wan, A. M. Turner, A. Vishwanath, and S. Y. Savrasov, Physical Review B **83**, 205101 (2011).
[13] P. Hosur and X. Qi, Comptes Rendus Physique **14**, 857 (2013).
[14] N. P. Armitage, E. J. Mele, and A. Vishwanath, Reviews of Modern Physics **90**, 015001 (2018).
[15] M. Berry and J. Robbins, Proc. R. Soc. Lond. A **442**, 641 (1993).
[16] M. Berry and J. Robbins, Proc. R. Soc. Lond. A **442**, 659 (1993).
[17] G. Sundaram and Q. Niu, Physical Review B **59**, 14915 (1999).
[18] D. Xiao, M.-C. Chang, and Q. Niu, Reviews of modern physics **82**, 1959 (2010).

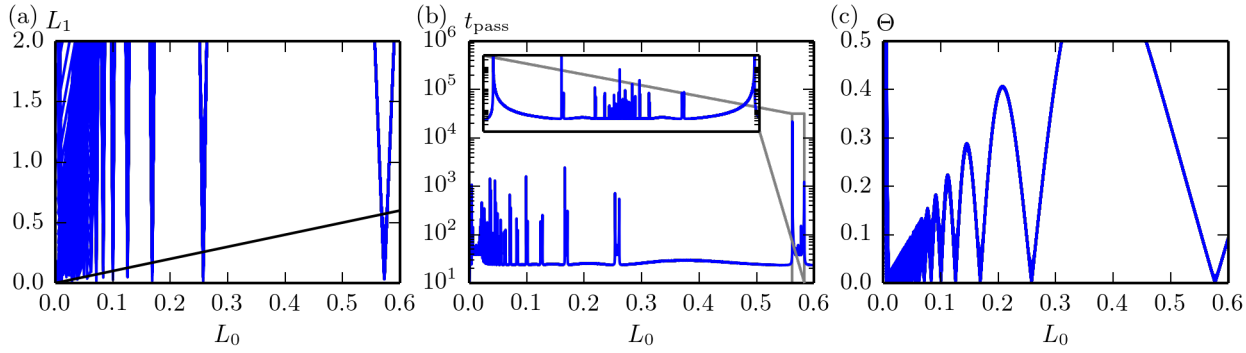

FIG. 14. L_1, $t_{\rm pass}$ and Θ as a function of L_0 at $A = B = 10$. As we can see, the peak of $t_{\rm pass}$ is near the region where $L_0 = L_1$ holds.

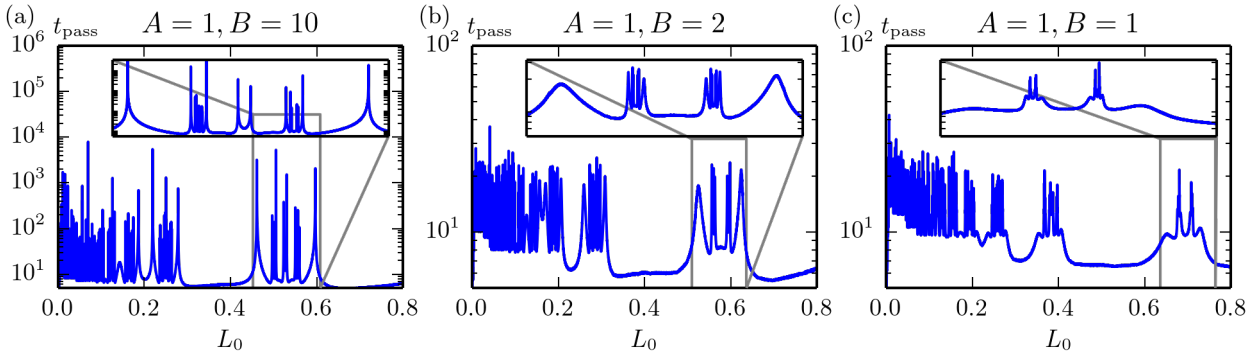

FIG. 15. L_1, $t_{\rm pass}$ and Θ as a function of L_0. As we can see, the peak of $t_{\rm pass}$ is near the region where $L_0 = L_1$ holds.

[19] P. Goddard and D. I. Olive, Reports on Progress in Physics **41**, 1357 (1978).
[20] J. Preskill, Annual Review of Nuclear and Particle Science **34**, 461 (1984).
[21] D. Tong, (2005), arXiv:0509216 [hep-th].
[22] Y. M. Shnir, *Magnetic Monopoles*, Text and Monographs in Physics (Springer, Berlin/Heidelberg, 2005).
[23] K. McDonald, "Birkeland, darboux and poincaré: Motion of an electric charge in the field of a magnetic pole (apr. 15, 2015),".
[24] G. Darboux, Bulletin des Sciences Mathmatiques et Astronomiques **2**, 433 (1878).
[25] H. Poincaré, Comptes Rendus Acad. Sci **123**, 530 (1896).
[26] C. Jung, Journal of physics A: mathematical and general **19**, 1345 (1986).
[27] B. Eckhardt, Journal of Physics A: Mathematical and General **20**, 5971 (1987).
[28] B. Eckhardt, Physica D: Nonlinear Phenomena **33**, 89 (1988).
[29] C. Jung and S. Pott, Journal of Physics A: Mathematical and General **22**, 2925 (1989).
[30] P. Gaspard and S. A. Rice, The Journal of Chemical Physics **90**, 2225 (1989).
[31] S. Bleher, C. Grebogi, and E. Ott, Physica. D, Nonlinear Phenomena **46**, 87 (1990).
[32] D. Xiao, M. C. Chang, and Q. Niu, Reviews of Modern Physics **82**, 1959 (2010).
[33] B. Simon, Physical Review Letters **51**, 2167 (1983).
[34] H. Goldstein, C. Poole, and J. Safko, *Classical mechanics* (2002).
[35] C. K. Birdsall and A. B. Langdon, *Plasma Physics Via Computer Simulation* (McGraw-Hill, Inc., 1985).
[36] E. Ott, *Chaos in Dynamical Systems* (Cambridge University Press, 2002).
[37] Y.-C. Lai and T. Tél, *Transient Chaos* (Springer, 2011).
[38] D. G. Boulware, L. S. Brown, R. N. Cahn, S. Ellis, and C. Lee, Physical Review D **14**, 2708 (1976).
[39] J. Schwinger, K. A. Milton, W.-Y. Tsai, L. L. DeRaad, and D. C. Clark, Annals of Physics **101**, 451 (1976).
[40] S. Smale, Bulletin of the American mathematical Society **73**, 747 (1967).
[41] Q. Chen, M. Ding, and E. Ott, Physics Letters A **145**, 93 (1990).
[42] H. Kantz and P. Grassberger, Physica D: Nonlinear Phenomena **17**, 75 (1985).
[43] P. Gaspard, *Chaos, scattering and statistical mechanics*, Vol. 9 (Cambridge University Press, 2005).
[44] L.-S. Young, Ergodic theory and dynamical systems **2**, 109 (1982).
[45] Y.-T. Lau, J. M. Finn, and E. Ott, Phys. Rev. Lett. **66**, 978 (1991).
[46] In other words, once the direction of $\vec{J}$ is fixed from Eq. (A2), then the opening angle is automatically determined from the requirement that the cone should be tangential

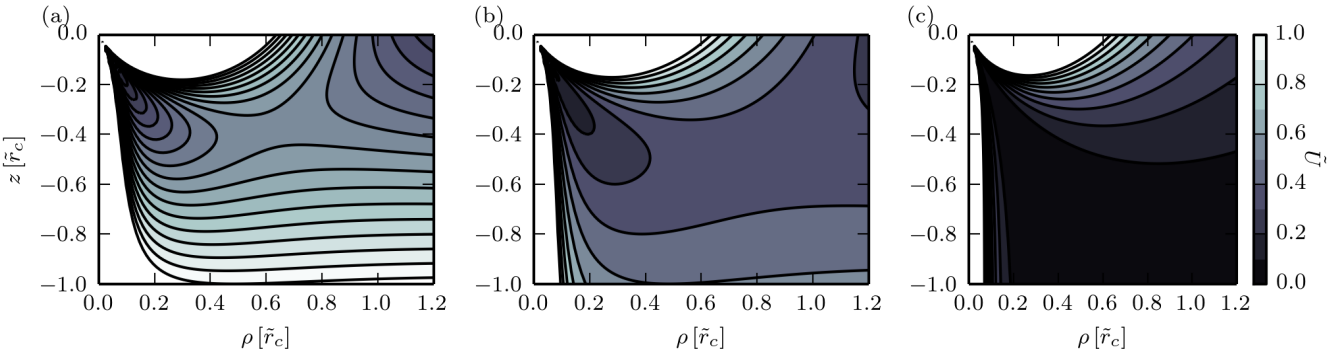

FIG. 16. The change of U_{eff} by varying the dimensionless force parameter, F. Here we set $J_z/(q_m q_e) = 0.9$, and (a) $F = 1$, (b) $F = 0.5$, (c) $F = 0$.

to the plane subtended by the vectors $\vec{r}_0$ and $\vec{v}_0$.

[47] H. E. Nusse and J. A. Yorke, Physica D: Nonlinear Phenomena **36**, 137 (1989).

[48] A. E. Motter and Y.-C. Lai, Physical Review E **65**, 015205 (2001).

[49] J. M. Seoane, J. Aguirre, M. A. Sanjuán, and Y.-C. Lai, Chaos: An Interdisciplinary Journal of Nonlinear Science **16**, 023101 (2006).

[50] J. M. Seoane, M. A. Sanjuán, and Y.-C. Lai, Physical Review E **76**, 016208 (2007).

[51] A. E. Motter, M. Gruiz, G. Károlyi, and T. Tél, Phys. Rev. Lett. **111**, 194101 (2013).

[52] X. Chen, T. Nishikawa, and A. E. Motter, Phys. Rev. X **7**, 021040 (2017).

[53] M. V. Berry and E. C. Sinclair, Journal of Physics A: Mathematical and General **30**, 2853 (1997).

[54] K. Nakamura, The Bulletin of arts and sciences, Meiji University **181**, 1 (1985).